On the dynamic behaviour of discrete metamaterials: From attenuation to energy localization

Marco Moscatelli, Claudia Comi, Jean-Jacques Marigo

Version of Record: https://www.sciencedirect.com/science/article/pii/S0165212521000317
Manuscript_67a35d50be6ee20fa1988de84a6990b1

On the dynamic behaviour of discrete metamaterials: from attenuation to energy localization

Marco Moscatelli[a,b,*], Claudia Comi[b], Jean-Jacques Marigo[a]

[a] *Laboratoire de Mécanique des Solides, École Polytechnique, Route de Saclay, 91120 Palaiseau, France*
[b] *Department of Civil and Environmental Engineering, Politecnico di Milano, Piazza Leonardo da Vinci 32, 20133 Milan, Italy*

Abstract

Metamaterials are generally known for their waves attenuation capabilities. This behaviour, which is related to the microstructure composing these materials, can be due to a Bragg-type scattering mechanism or to local resonances. The objective here is to exploit the two phenomena for generating a system able to localize the energy carried by propagating elastic (or acoustic) waves. To this purpose, we employ a 1D lattice composed of a chain of mass-in-mass particles, connected by elastic springs. The lattice contains an internal defect that causes the energy localization. This configuration allows for a completely analytical description of the problem. Eventually, an extensive discussion on the interaction between the two attenuation mechanisms is also given.

Keywords: metamaterial, energy harvesting, wave localization, lattice, effective mass

1. Introduction

Metamaterials are composites made up of a periodic repetition of a unit cell, itself containing a microstructure. A widely studied feature of this class of materials is the presence of band gaps affecting their dynamic response, *i.e.* gaps of frequencies at which waves cannot propagate. This behaviour was first noticed in the field of electromagnetism, leading to the development of photonic crystals [1]. Very soon, these studies were extended to the field of elasticity and acoustics, with the emergence of the so-called *Phononic Crystals* (PCs) and *Locally Resonant Materials* (LRMs) (very often, LRMs are named *Acoustic Metamaterials* in the literature. For a detailed review of both categories see *e.g.* [2] and [3]).

In the present work we use the general term *metamaterial* to indicate both PCs and LRMs, as suggested in [4]. The distinction between these two specific classes of metamaterials is nevertheless kept because of the different nature of the mechanisms responsible for the attenuation of propagating waves.

*Corresponding author
Email addresses: marco.moscatelli@polytechnique.edu (Marco Moscatelli), claudia.comi@polimi.it (Claudia Comi), jean-jacques.marigo@polytechnique.edu (Jean-Jacques Marigo)

Metamaterials are often composed of a matrix with periodically distributed inclusions. The presence of a microstructure can then cause the formation of band gaps. In PCs, the scatterers contained in each unit cell behave exactly as the rectangular potential wells in a Kronig-Penney model, usually employed for studying the motion of electrons in solids [5]. Band gaps are thus induced by a Bragg-type scattering, caused by a destructive interference of Bloch waves. In LRMs, wave cancellation is due to Fano-like interactions [6, 7] between the macroscopic waves propagating in the matrix and the local eigenvibrations of the microstructure [8]. Mie [9], Helmohltz [10, 11] or Minneart [12] local resonances govern the response of the system and band gaps can occur at wavelengths well above the spacing of the lattice.

Bragg scattering is generally disregarded when dealing with LRMs. Some authors have studied *Hybrid Metamaterials* (HMs), with the aim of obtaining an interaction between the two mechanisms of attenuation [13]. This phenomenon has offered the opportunity of broadening the band gaps [14, 15].

A rather common and efficient way to investigate band gaps formation consists in using discrete systems. Crystal-type structures composed of lumped masses connected by springs are mainly constructed for analysing the mechanism of Bragg scattering in PCs [16, 17]. Mass-in-mass lattices are instead generally employed for LRMs [18–21], also allowing for a direct implementation of materials non linearities [22–25] [1].

The formation of band gaps in mass-in-mass models is usually interpreted in terms of an effective mass, that becomes negative at specific frequencies intervals [26–28]. This is also in accordance to what is found through homogenization for continuous LRMs, when soft inclusions are periodically dispersed in a stiff matrix [29–31]. However, this result remains true only when the ratio between the stiffness of the inner resonator and that of the outer springs is small. The case where the stiffness of the resonator is of the same order or higher than that of the outer spring is usually disregarded for mass-in-mass lattices.

A number of applications of the peculiar dynamic behaviour of metamaterials have been studied in the literature ([32–35] to mention but a few). In particular, wave localization is an important aspect that has been greatly investigated in the past for crystals [36, 37] and that has become again popular with the advent of metamaterials [38–41]. Breaking the discrete translational symmetry by inserting a defect can trap waves that are trying to propagate through the system, generating a so-called *defect state*. This phenomenon has been exploited first in [42] and then in [43] for designing PCs with a point defect, that are capable of harvesting respectively the energy carried by acoustical and mechanical waves. Lately, more energy harvesting systems based on defect states have appeared [44–46].

In [47–49] systems for the localization of the mechanical energy carried by propagating elastic waves are proposed. These systems combine the behaviour of a Fabry-Pérot interferometer with the wave localization in continuous LRMs. In [50], a one-dimensional discrete

[1] This mechanical model has an interpretation also in acoustics: masses and the springs represent respectively the density and the elastic modulus of compression of air in an acoustical context. Moreover, when scalar waves are considered, elastic and pressure wave equations are formally equivalent, with simply an inversion of the role played by the material properties.

counterpart of the above systems is described and numerically studied to show the influence of the number of the mass-in-mass cells and of the defect width on the wave localization. The metamaterial is there interpreted as a discrete version of a LRM.

In the same line of research, in the present work we focus on discrete mass-in-mass systems and we derive new complete analytical results concerning band-gap formation and energy localization inside a cavity. At difference from previous literature, no a-priori restrictions are imposed on stiffness and mass ratios of the lattice. First, we derive in close form the conditions on the material parameters under which a Bragg-type mechanism or a locally resonant mechanism lead to band-gap formation, thus fixing the limit of validity of the effective models widely used in the literature. More specifically, we show that mass-in-mass lattices can be interpreted as discrete versions of HMs. Then the dynamic response of a system with a defect, similar to the one numerically studied in [50], is analytically characterized. The conditions for optimal energy localization inside the defect are found: the localization can be obtained not only by means of local resonances inside the metamaterial, but also through the mechanism of Bragg scattering. These results can be exploited for the design of energy harvesters.

The plan of the paper is as follows. In section 2, we consider the band gaps associated with the mass-in-mass 1D chain, by analysing their dependence on the mass and stiffness ratios. Then we compare the results with those coming from the corresponding continuous one-dimensional metamaterial, showing the reason of the differences. Finally, we treat the case of a simple mass-spring chain. In section 3, we describe the discrete system for energy localization constituted by a mass-spring chain with two mass-in-mass barriers delimiting a central defect, and we analytically derive its dynamic behaviour. In section 4, we compute the mechanical energy density for the two lattice types under consideration (namely the mass-in-mass chain and the mass-spring chain). Fixing some of the parameters governing the problem, we study the localization phenomenon and we show how the presence of a defect dramatically affects the behaviour of the system, both in the frequency and time domain. Eventually, in section 5 conclusions are drawn.

2. The discrete mass-in-mass lattice

Let us first consider the mass-in-mass chain, shown in figure 1. The system is composed of a periodic repetition of external masses m_1 which are connected to the nearest neighbor masses with springs k_1 and contain internal resonating masses m_2, attached with springs k_2. Note that, for the sake of symmetry, the chosen unit cell shown in figure 1 includes mass m_1 with the internal resonator (of mass m_2 and stiffness k_2) and two springs of stiffness $k_1/2$. The size of the unit cell is ℓ. Each spring is considered as massless. The index $j \in \mathbb{Z}$ is used for referring to a particular cell in the chosen numbering. The displacements of the external and internal masses will be denoted by u_j and v_j respectively.

For the sake of clarity, we will consider the problem of elastic waves propagation, nevertheless, everything that follows applies also to the acoustic case, with a suitable reinterpretation of the quantities. The angular frequency ω will be called just frequency in the rest of the paper.

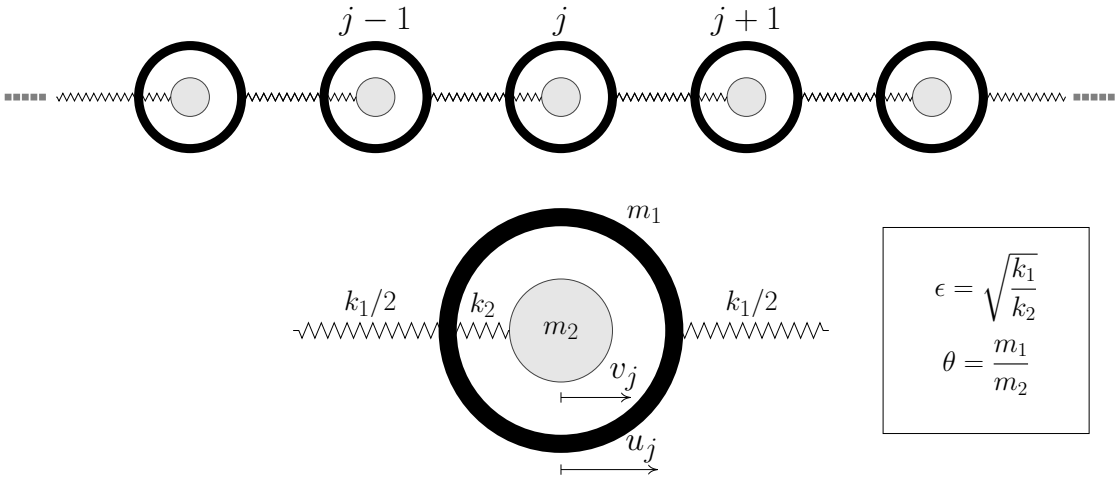

Figure 1: sketch of the mass-in-mass chain and zoom over its microstructure. Masses m_1 are connected to the nearest neighbors with springs k_1 on both sides. Each mass m_1 contains a resonator m_2 connected with spring k_2. The chosen unit cell includes mass m_1 with the internal resonator and two springs of stiffness $k_1/2$.

2.1. Formulation of the motion problem

Studying the motion of the mass-in-mass chain described in figure 1 leads to the following differential system:

$$\begin{cases} m_1 \ddot{u}_j = k_1 \Delta_j u + k_2(v_j - u_j) \\ m_2 \ddot{v}_j = k_2(u_j - v_j) \end{cases} \tag{1}$$

where Δ_j denotes the discrete differential operator

$$\Delta_j u = u_{j+1} + u_{j-1} - 2u_j \tag{2}$$

and superposed dots mark time derivatives.

We will only consider motions at a given frequency ω, so that the variation in time t of the displacement can be expressed as

$$u_j(t) = U_j \exp(\mathrm{i}\omega t), \qquad v_j(t) = V_j \exp(\mathrm{i}\omega t)$$

and hence the system (1) becomes:

$$\begin{cases} m_1\omega^2 U_j + k_1 \Delta_j U + k_2(V_j - U_j) = 0 \\ m_2\omega^2 V_j + k_2(U_j - V_j) = 0 \end{cases} \tag{3}$$

Let us introduce the eigenfrequencies

$$\omega_1 = \sqrt{\frac{k_1}{m_1}}, \quad \omega_2 = \sqrt{\frac{k_2}{m_2}}$$

and the following dimensionless (positive) quantities:

$$\Omega = \frac{\omega^2}{\omega_2^2}, \qquad \varepsilon = \sqrt{\frac{k_1}{k_2}}, \qquad \theta = \frac{m_1}{m_2}.$$

Inserting them into Eqs. (3) leads to:

$$\begin{cases} \theta\Omega U_j + \varepsilon^2 \Delta_j U + (V_j - U_j) = 0 \\ \Omega V_j + (U_j - V_j) = 0 \end{cases} \tag{4}$$

The second of Eqs. (4) gives V_j in terms of U_j (provided that $\Omega \neq 1$):

$$V_j = \frac{U_j}{1-\Omega} \tag{5}$$

and inserting that relation into the first of Eqs. (4) gives the discrete differential equation governing the motion of U:

$$\varepsilon^2 \Delta_j U + \mu_\theta(\Omega) U_j = 0 \quad \text{with} \quad \mu_\theta(\Omega) = \theta\Omega + \frac{1}{1-\Omega} - 1. \tag{6}$$

Hence at given Ω, the motion depends on the two parameters θ and ε. The case of a stiff inclusion embedded in a soft matrix corresponds to small ε, and the opposite case, *i.e.* soft-in-stiff, to large ε. Therefore, this system can in principle be used as a simplified model exhibiting both Bragg scattering and local resonance.

Let us study the properties of the function $\Omega \mapsto \mu_\theta(\Omega)$ (at given mass ratio θ) which can be interpreted as the (dimensionless) effective mass, multiplied by the dimensionless (positive) frequency Ω. From the second of relations (6), one sees that μ_θ is monotonically increasing in its domain of definition, as shown in figure 2.

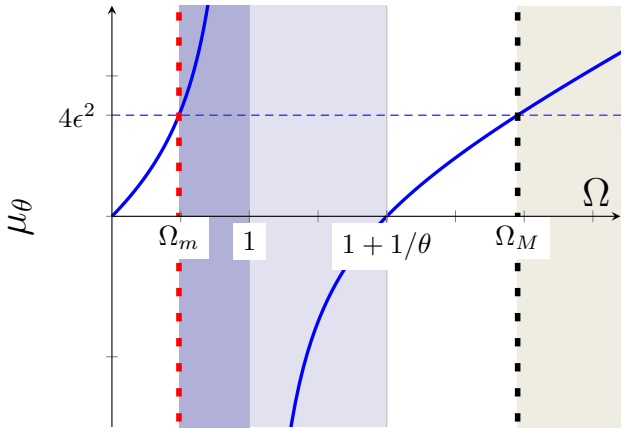

Figure 2: variation of $\mu_\theta(\Omega)$ with θ and band gaps. Intervals $[\Omega_m, 1+1/\theta]$ and $[\Omega_M, +\infty)$ denote the two band gaps: $[\Omega_m, 1]$ (darker blue) and $[\Omega_M, +\infty)$ (gray) are due to Bragg scattering; $[1, 1+1/\theta]$ (lighter blue) is due to local resonances. By varying ε, the vertical dashed lines move and the band gaps due to Bragg scattering get either wider or narrower when ε becomes respectively smaller and larger. The part of the first band gap generated by local resonances can be modified only by varying θ.

Specifically, one obtains that μ_θ is always increasing with Ω and is negative in the interval $(1, 1 + 1/\theta)$ of Ω. This interval corresponds to the formation of a band gap due to local resonances, as discussed *e.g.* in [29] and [31].

2.2. General solutions and band gaps

The general solution of Eq. (6) can be obtained in closed form. Let us search the solution in the form $U_j = r^j$ with r to be determined. Inserting it into Eq. (6) gives the following second degree equation for r:

$$r^2 - 2br + 1 = 0 \quad \text{with} \quad b = 1 - \frac{\mu_\theta(\Omega)}{2\varepsilon^2}. \tag{7}$$

Therefore the roots will be real for $|b| \geq 1$ and complex for $|b| < 1$. Let us consider each case separately.

(i) $0 < \mu_\theta(\Omega) < 4\varepsilon^2$. In that case, $|b| < 1$ and the two roots are complex conjugate. Let us set

$$b = \cos \mathsf{K}^* \quad \text{with} \quad \mathsf{K}^* \in (0, \pi).$$

Then the two roots are $r = \cos \mathsf{K}^* \pm \mathsf{i} \sin \mathsf{K}^* = \exp(\pm \mathsf{i}\mathsf{K}^*)$ and the general solution of Eq. (6) reads

$$U_j = a_1 \cos j\mathsf{K}^* + a_2 \sin j\mathsf{K}^*, \tag{8}$$

where a_1 and a_2 are two arbitrary constants fixed by boundary conditions.

(ii) $\mu_\theta(\Omega) < 0$. In that case, $b > 1$ and the two roots are real numbers. Let us set

$$b = \mathrm{ch}\, \mathsf{K}^* \quad \text{with} \quad \mathsf{K}^* > 0.$$

Then the two roots are $r = \mathrm{ch}\, \mathsf{K}^* \pm \mathrm{sh}\, \mathsf{K}^* = \exp(\pm \mathsf{K}^*)$ and the general solution of Eq. (6) reads

$$U_j = a_1 \mathrm{ch}\, j\mathsf{K}^* + a_2 \mathrm{sh}\, j\mathsf{K}^*. \tag{9}$$

(iii) $\mu_\theta(\Omega) > 4\varepsilon^2$. In that case, $b < -1$ and the two roots are real numbers again. Setting

$$b = -\mathrm{ch}\, \mathsf{K}^* \quad \text{with} \quad \mathsf{K}^* > 0$$

the two roots are $r = -\mathrm{ch}\, \mathsf{K}^* \pm \mathrm{sh}\, \mathsf{K}^* = -\exp(\pm \mathsf{K}^*)$ and the general solution of Eq. (6) reads

$$U_j = a_1 (-1)^j \mathrm{ch}\, j\mathsf{K}^* + a_2 (-1)^j \mathrm{sh}\, j\mathsf{K}^*. \tag{10}$$

Note that, when $|b| = 1$ (*i.e.* when $\mu_\theta = 0$ or $4\varepsilon^2$), the solutions of Eq. (7) are double roots. For this particular case, one can check that the general solution of Eq. (6) becomes:

$$U_j = \begin{cases} a_1 + j a_2 & \text{when } \mu_\theta = 0 \\ (-1)^j (a_1 + j a_2) & \text{when } \mu_\theta = 4\varepsilon^2 \end{cases}$$

This can be verified either by looking at the limiting behaviours of relations (8), (9) and (10), or by directly looking for a second solution of Eq. (6) in the form $U_j = j r^j$.

Let us now describe more in details the three different behaviours (i), (ii) and (iii). The solution corresponds to propagating waves only in the case (i) and hence the two other cases (ii) and (iii) give the band gaps. Accordingly, the band gaps correspond to the intervals of Ω such that $\mu_\theta(\Omega) < 0$ or $\mu_\theta(\Omega) > 4\varepsilon^2$. The first condition corresponds to the interval $(1, \Omega_0 = 1 + 1/\theta)$ where the effective mass is negative (see figure 2). There exists two values of Ω, say Ω_m and Ω_M, such that $\mu_\theta(\Omega) = 4\varepsilon^2$. Specifically, Ω_m and Ω_M are the two roots of the second degree equation

$$\theta\Omega^2 - (1 + \theta + 4\varepsilon^2)\Omega + 4\varepsilon^2 = 0 \tag{11}$$

and read:

$$\begin{cases} \Omega_m = \dfrac{1}{2\theta}\left(1 + \theta + 4\varepsilon^2 - \sqrt{(1 + \theta - 4\varepsilon^2)^2 + 16\varepsilon^2}\right) \\ \Omega_M = \dfrac{1}{2\theta}\left(1 + \theta + 4\varepsilon^2 + \sqrt{(1 + \theta - 4\varepsilon^2)^2 + 16\varepsilon^2}\right) \end{cases} . \tag{12}$$

The first root Ω_m belongs to the interval $(0, 1)$ and the second one Ω_M is greater than Ω_0. When $\Omega = 1$, one sees directly in system (4) that $U_j = V_j = 0$ and no motion is possible. Hence, the band gaps correspond to the two intervals $[\Omega_m, \Omega_0]$ and $[\Omega_M, +\infty)$, shown in figure 2.

The dependence of Ω_m, Ω_0 and Ω_M on the two parameters ε and θ is studied respectively in figures 3 and 4. Each panel composing the two figures contains three curves representing the behaviour of the three frequencies under consideration, in particular: Ω_m is indicated in red, Ω_0 in blue and Ω_M in black. The filled areas denote instead the two band gaps previously defined. Two different colors have been used for the first band gap, in order to distinguish between the part of the band gap where the effective mass is positive (darker region) from that where it is negative (lighter region). In the following, we will refer to the lower and upper parts of the first band gap as "band gap A" and "band gap B", respectively.

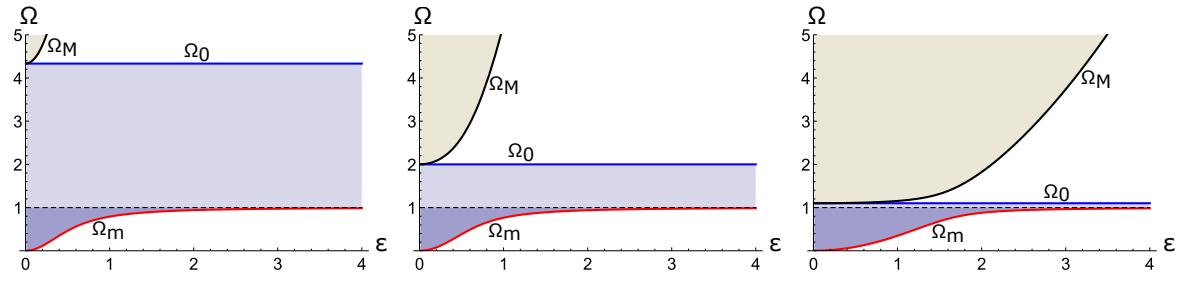

(a) $\theta = 0.3$. (b) $\theta = 1$. (c) $\theta = 10$.

Figure 3: dependence of Ω_m (in red), Ω_0 (in blue) and Ω_M (in black) on ε. The parameter θ is fixed to 0.3 (3a), 1 (3b) and 10 (3c). Filled areas correspond to band gaps.

As it is clear in both figure 3 and 4, the frequency Ω_0 is independent from the ratio ε between the stiffnesses of the springs and decreases as the mass ratio θ increases. In particular, it is responsible for the width of band gap B. As stated before, this band gap is indeed caused by the presence of local resonances. It is thus reasonable that, when θ is

large, *i.e.* when the mass of the resonator m_2 is small with respect to m_1, the effect of the resonance is reduced, resulting in a thinner band gap B.

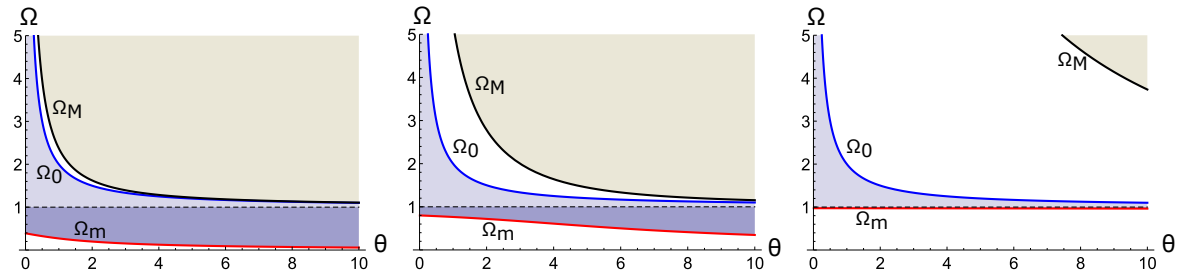

(a) $\varepsilon = 0.4$. (b) $\varepsilon = 1$. (c) $\varepsilon = 3$.

Figure 4: dependence of Ω_m (in red), Ω_0 (in blue) and Ω_M (in black) on θ. The parameter ε is fixed to 0.4 (4a), 1 (4b) and 3 (4c). Filled areas correspond to band gaps. Ω_0 is independent from ε, hence the same curve appears in the three plots.

The frequency Ω_m governs the width of band gap A. The presence of this band gap is not due to local resonances, being μ_θ positive. Band gap A is generated by a mechanism of Bragg scattering, although it appears connected with a band gap coming from local resonances. As stated in the introduction, this feature is typical of a *hybrid metamaterial* (HM), where the phenomena of Bragg scattering and local resonance are coupled to enlarge the band gap width [13].

From figure 3, one can note that Ω_m tends to 1 as ε grows, causing the reduction of the width of band gap A: in the limit band gap A vanishes. This can be explained as follows: increasing ε, the stiffness k_2 of the internal resonator becomes smaller than k_1 and the system resembles very much a discrete version of a *locally resonant material* (LRM), whose dynamic response is well known to be governed by local resonances. The behaviour of the frequency Ω_M, responsible for the opening of the second band gap, confirms the last remark: its value increases with ε, for a fixed θ, and the second band gap thus opens for higher frequencies and in the limit tends to disappear. If high values of the stiffness ratio ε are considered, as often done in the literature (see *e.g.* [23, 26, 28]), only this latter case is of interest.

The influence of the parameter θ on Ω_m is limited (see figure 4), especially for large values of ε. Ω_M, similarly to Ω_0, decreases with θ.

We have thus shown here that a mass-in-mass chain, albeit generally used only for modelling LRMs, it is nevertheless a HM. Therefore the mass-in-mass chain, properly tuned, can be used to study a system governed by either one of the two wave cancelling mechanisms or both.

It is particularly interesting to discuss the structure of the stop and pass bands in the limit cases of ε tending to ∞ or ε tending to zero. The asymptotic behaviour of Ω_m and Ω_M can be obtained directly from Eq. (11). When ε is large, the solution(s) of Eq. (11), denoted by Ω^ε, can be expanded as follows:

$$\Omega^\varepsilon = \varepsilon^2 \Omega^{(2)} + \Omega^{(0)} + \varepsilon^{-2} \Omega^{(-2)} + \cdots$$

and inserting into Eq. (11) gives:

$$\begin{cases} \Omega^{(2)}\left(\theta\Omega^{(2)}-4\right)=0 & \text{at the order of } \varepsilon^4 \\ 2\theta\Omega^{(2)}\Omega^{(0)}-(1+\theta)\Omega^{(2)}-4\Omega^{(0)}+4=0 & \text{at the order of } \varepsilon^2 \\ \theta{\Omega^{(0)}}^2+2\theta\Omega^{(2)}\Omega^{(-2)}-(1+\theta)\Omega^{(0)}-4\Omega^{(-2)}=0 & \text{at the order of } \varepsilon^0 \end{cases}$$

The expansion of Ω_m corresponds to $\Omega^{(2)}=0$ and hence

$$\Omega_m = 1-\frac{1}{4\varepsilon^2}+\cdots$$

whereas the expansion of Ω_M corresponds to $\Omega^{(2)}=4/\theta$ and hence

$$\Omega_M = \frac{4\varepsilon^2}{\theta}+\frac{1}{\theta}+\frac{1}{4\varepsilon^2}\cdots$$

When ε goes to infinity, the first band gap tends to the interval $[1,\Omega_0]$ which corresponds to negative effective mass. One recovers the results obtained in the soft-in-stiff case, with band gaps generated by local resonances. In terms of the physical quantities, this (asymptotic) band gap is given by

$$\text{band gap in the soft-in-stiff case:}\quad \omega\in\left[\omega_2,\omega_2\sqrt{1+\frac{m_2}{m_1}}\right].$$

When ε is small, Ω^ε can be expanded as $\Omega^\varepsilon=\Omega^{(0)}+\varepsilon^2\Omega^{(2)}+\cdots$. Inserting it into Eq. (11) gives:

$$\begin{cases} \Omega^{(0)}\left(\theta\Omega^{(0)}-1-\theta\right)=0 & \text{at the order of } \varepsilon^0 \\ 2\theta\Omega^{(0)}\Omega^{(2)}-(1+\theta)\Omega^{(2)}-4\Omega^{(0)}+4=0 & \text{at the order of } \varepsilon^2 \end{cases}$$

The expansion of Ω_m corresponds to $\Omega^{(0)}=0$ and hence

$$\Omega_m = \frac{4\varepsilon^2}{1+\theta}+\cdots$$

whereas the expansion of Ω_M corresponds to $\Omega^{(0)}=1+1/\theta=\Omega_0$ and hence

$$\Omega_M = 1+\frac{1}{\theta}+\frac{4\varepsilon^2}{\theta(1+\theta)}+\cdots$$

Therefore, almost all frequencies are forbidden except two small intervals of allowed frequencies, the first close to 0 and the other to Ω_0, see figure 3. In terms of the physical quantities, the allowed intervals are (approximately) given by

$$\text{first propagating band in the stiff-in-soft case:}\quad \omega\in\left(0,\frac{2\omega_1}{\sqrt{1+\dfrac{m_2}{m_1}}}\right),$$

$$\text{second propagating band:} \quad \omega - \omega_2\sqrt{1+\frac{m_2}{m_1}} \in \left(0, \frac{2\omega_1}{\sqrt{1+\frac{m_1}{m_2}}}\right).$$

In this case, band gaps are generated not only by local resonances (for which the effective mass is negative) but also by Bragg reflections of the propagating waves.

2.3. Comparison with the continuous model and the Bloch-Floquet solution

Let us now consider the wave propagation in the one dimensional continuous counterpart of the discrete mass-in-mass chain. The continuous model can be thought of as the limit of the discrete one when the internal length is small with respect to the wave length. The Helmholtz equation in this case can be obtained by replacing in Eq. (4) the discrete differential operator $\Delta_j U$ by the second derivative with respect to the spatial variable x, obtaining

$$\varepsilon^2\ell^2 U''(x) + \mu_\theta(\Omega)U(x) = 0 \tag{13}$$

where ℓ is a characteristic length, which is introduced for dimensional reasons and is related to the size of the microstructure. The general solution of Eq. (13) depends on the sign of $\mu_\theta(\Omega)$: (i) if the effective mass is positive, then the general solution is sinusoidal in space; (ii) if the effective mass is negative, then the general solution is exponential in space. Therefore, the band gap is given by the interval $[1, \Omega_0]$, closure of the interval where the effective mass is negative, whatever the value of ε. This result is completely different from that of the discrete model, especially for small values of ε. The reason can be understood by considering the Bloch-Floquet approach.

Let us start from the discrete model. In the Bloch-Floquet approach, the motion is searched under the form $U_{j+1} = U_j \exp \mathsf{i}\kappa\ell$ where κ is the given wave number and ℓ the cell size. Inserting this form into Eqs. (4) gives the dispersion equation relating the frequency to the wave number:

$$4\varepsilon^2 \sin^2 \frac{\kappa\ell}{2} = \mu_\theta(\Omega). \tag{14}$$

Therefore, at given κ, a solution exists for Ω only if $0 \leq \mu_\theta(\Omega) \leq 4\varepsilon^2$ and one recovers the results of section 2.2.

If we consider now the continuous model (13) and motions of the form $U(x+\ell) = U(x)\exp \mathsf{i}\kappa\ell$, the dispersion relation becomes

$$\varepsilon^2\kappa^2\ell^2 = \mu_\theta(\Omega). \tag{15}$$

At given $\kappa \neq 0$ there exist two solutions for Ω, one in the interval $(0,1)$, the other in the interval $(\Omega_0, +\infty)$. When κ goes from 0 to infinity, the two solutions describe those two intervals, therefore the band gap corresponds to the interval $[1, \Omega_0]$.

If we compare Eq. (14) with Eq. (15), it appears that Eq. (15) can be seen as an approximation of Eq. (14) for small values of $\kappa\ell$. So the continuous model is a good representation of the discrete model for small wave numbers (large wave lengths) but not for small wave lengths. It should be used only when the ratio $\kappa\ell/2\pi$ is small (with respect to 1). If it is

used for any value of $\kappa\ell$, there are some differences with the discrete model, that depend on ε. Specifically, let us consider the two cases according to ε is large or small.

- *Large ε.* In this case the whole interval $(0, +\infty)$ of the left hand side of Eqs. (14) and (15) can be spanned by small values of $\kappa\ell$ (for instance $\kappa\ell \sim \varepsilon^{-1/2}$). Hence, when ε goes to infinity both models give $[1, \Omega_0]$ as the band gap.

- *Small ε.* For the discrete model, the left hand side of Eq. (14) remains small for any value of $\kappa\ell$ and hence Ω must be close to the two roots of μ_θ. But for the continuous model, if one considers any value of $\kappa\ell$, then the left hand side of Eq. (15) describes all the interval $(0, +\infty)$ even if ε is small and the band gap is still $[1, \Omega_0]$.

2.4. The spring-mass chain

Let us now consider the classical spring-mass chain. This model will be useful later on in the paper for properly representing the discrete counterpart of a homogeneous material. The lattice can be obtained by considering only masses m_1 connected by springs k_1. In this way, we are modeling the discrete counterpart of a continuous system composed by the same material used for the matrix of the metamaterial previously described. For this case, the motion problem is governed by the following equation:

$$m_1 \ddot{u}_j = k_1 \Delta_j u, \tag{16}$$

with $\Delta_j u$ still defined by the relation (2). Considering waves at given frequency ω and using the same notation of section 2.1, in terms of dimensionless quantities, Eq. (16) can be rewritten as

$$\varepsilon^2 \Delta_j U + \theta\Omega U_j = 0. \tag{17}$$

This Helmholtz equation has the same form of Eq. (6), with $\mu_\theta(\Omega)$ replaced by $\theta\Omega$.

Using the same procedure shown in section 2.2, when considering the matrix alone, the motion corresponds to propagating waves only when

$$0 < \Omega < \frac{4\varepsilon^2}{\theta}.$$

In such a case, setting

$$\frac{\theta\Omega}{2\varepsilon^2} = 1 - \cos \mathsf{K} \quad \text{with} \quad \mathsf{K} \in (0, \pi), \tag{18}$$

the general solution of Eq. (17) is given by

$$U_j = a_1 \cos j\mathsf{K} + a_2 \sin j\mathsf{K} \tag{19}$$

where a_1 and a_2 are arbitrary constants.

3. The spring-mass chain with two mass-in-mass barriers

3.1. Problem definition

We analyse the system shown in figure 5, with five regions made of springs k_1 and masses m_1 either alone (spring-mass chain) or connected to masses m_2 by springs k_2 (mass-in-mass chain). The regions of the first type, corresponding to the matrix, are the regions Ⅰ, Ⅲ and Ⅴ; those of the second type, corresponding to the metamaterial (matrix with inclusions), are the regions Ⅱ and Ⅳ; the region Ⅲ (or "defect") is inserted between regions Ⅱ and Ⅳ, which can be thought of as "barriers". We assume that each metamaterial region contains n cells and the defect only one. As before, the number above a cell represents its index $j \in \mathbb{Z}$ in the chosen numbering. We consider an incoming wave in the region Ⅰ which propagates at the angular frequency ω with an amplitude 1, and we search the response in the five regions.

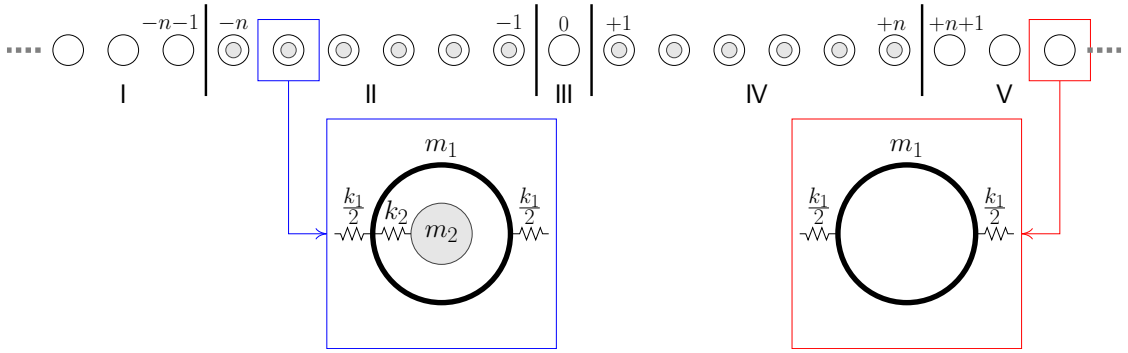

Figure 5: sketch of the studied system, with unit cells of the metamaterial and of the matrix. In parts Ⅰ and Ⅴ, the chain of masses m_1 and springs k_1 is infinitely extended for $j \to \pm\infty$. Regions Ⅱ and Ⅳ are composed of n cells each.

For localizing the energy carried by an incoming wave inside the defect, the propagation must be inhibited outside it, hence we consider Ω inside a band gap of the metamaterial and in the passband of the matrix, *i.e.*

$$\Omega < \frac{4\varepsilon^2}{\theta} \quad \text{and} \quad \Omega \in (\Omega_m, \Omega_0) \cup (\Omega_M, +\infty). \tag{20}$$

Taking into account relation (12) of Ω_m and Ω_M, one has $4\varepsilon^2/\theta = \Omega_m\Omega_M$, and since $\Omega_m < 1 < \Omega_M$, the following inequalities hold:

$$\Omega_m < \frac{4\varepsilon^2}{\theta} < \Omega_M. \tag{21}$$

Therefore, to comply with conditions (20), Ω must be chosen such that

$$\Omega_m < \Omega < \min\left\{1 + \frac{1}{\theta}, \frac{4\varepsilon^2}{\theta}\right\}. \tag{22}$$

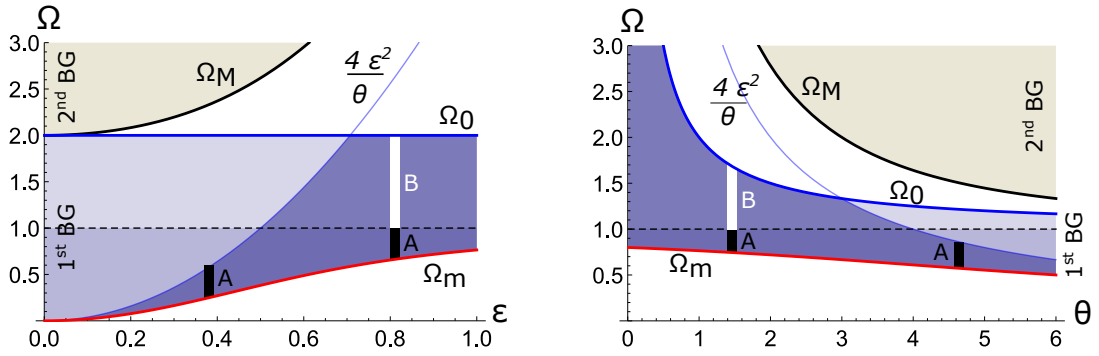

(a) $\theta = 1$. (b) $\varepsilon = 1$.

Figure 6: study of condition (22) with respect to ε (6a) and θ (6b) for respectively $\theta = 1$ and $\varepsilon = 1$. Band gaps are denoted by the filled areas. The darkest regions indicate all the frequencies which fulfill condition (22). Letters A and B are used for denoting frequencies respecting condition (22) and belonging to band gaps.

Condition (22) depends on ε and θ: by fixing one of the two parameters, the variation of the interval of frequencies respecting (22) can be studied with respect to the other parameter. This is done in figure 6a and 6b, where we fixed $\theta = 1$ and $\varepsilon = 1$ respectively. These two figures are a zoom near the origin of figures 3b and 4b. The frequencies fulfilling condition (22) are those inside the darkest regions in figure 6 and, hence, can belong to either band gap A or B, composing the first band gap. This means that, by properly fixing the parameters ε and θ, one can choose whether to exploit a Bragg mechanism (condition A) or a locally resonant mechanism (condition B) for generating the localization phenomenon.

In what follows, we consider both conditions. Two situations can arise: when $4\varepsilon^2 > \theta$, one can work with frequencies belonging either to band gap A or B (although for $\varepsilon >> 1$, band gap A disappears since $\Omega_m \to 1$); when $4\varepsilon^2 \leq \theta$, one has that $\Omega \leq 4\varepsilon^2/\theta \leq 1$ and localization can only be generated by a Bragg mechanism.

3.2. The motion of the system

All the calculations are carried out in the plane of complex numbers. The conjugate of c is denoted $\bar{c}$, its modulus $|c|$, its real part $\mathcal{R}e(c)$ and its imaginary part $\mathcal{I}m(c)$.

1. In the region I, using Eq. (17) and the definition (18) of K, the displacement U_j^{I} can be written as

$$U_j^{\mathsf{I}} = \mathsf{A}^{\mathsf{I}}\, e^{-\mathrm{i}\mathsf{K}(j+n+1)} + \mathsf{B}^{\mathsf{I}}\, e^{\mathrm{i}\mathsf{K}(j+n+1)}, \quad j < -n, \tag{23}$$

the first term corresponding to the incoming wave with a known amplitude A^{I} (propagating from the left to the right, in the direction of the increasing j's), the second one to the reflected wave propagating in the opposite direction and whose amplitude $\mathsf{B}^{\mathsf{I}} = \mathsf{R}$ has to be determined. Without loss of generality, we here consider $\mathsf{A}^{\mathsf{I}} = 1$. Substituting relation (23) into Eq. (17) written for $j = -n-1$ and accounting for relation (18), one obtains $U_{-n}^{\mathsf{I}} = e^{-\mathrm{i}\mathsf{K}} + \mathsf{R}\, e^{\mathrm{i}\mathsf{K}}$. Therefore, the expression (23) is also valid for $j = -n$ and this can be thought of as a continuity condition for the field U. Rewriting relation (23)

for $j = -n-1$ and for $j = -n$, one gets

$$U^{\mathsf{I}}_{-n-1} = 1 + \mathsf{R}, \qquad U^{\mathsf{I}}_{-n} = e^{-\mathsf{i}\mathsf{K}} + \mathsf{R}\, e^{\mathsf{i}\mathsf{K}}. \tag{24}$$

2. In the region II, the general solution of Eq. (6) is given by relations (9) or (10) according to whether $\mu_\theta(\Omega) < 0$ or $\mu_\theta(\Omega) > 4\varepsilon^2$.

   A When $\Omega < 1$, the general solution is given by relation (10). Accordingly, in region II the displacement can be written as

   $$U^{\mathsf{II}}_j = \mathsf{A}^{\mathsf{II}}\,(-1)^{j+n+1}\mathrm{ch}\,\mathsf{K}^*(j+n+1) + \mathsf{B}^{\mathsf{II}}\,(-1)^{j+n+1}\mathrm{sh}\,\mathsf{K}^*(j+n+1), \tag{25}$$

   where A^{II} and B^{II} have to be determined and $-n-1 \le j \le 0$. Note that relation (25) can still be used for $j = -n-1$ and $j = 0$, *i.e.* for the last point in the region I of the matrix and for the point of the defect. This is a continuity condition for U and using it for $j = -n-1$ and $j = -n$ gives $U^{\mathsf{II}}_{-n-1} = \mathsf{A}^{\mathsf{II}}$ and $U^{\mathsf{II}}_{-n} = -\mathsf{A}^{\mathsf{II}}\,\mathrm{ch}\,\mathsf{K}^* - \mathsf{B}^{\mathsf{II}}\,\mathrm{sh}\,\mathsf{K}^*$. Comparing with relations (24) one has

   $$\mathsf{A}^{\mathsf{II}} = 1 + \mathsf{R} \qquad \mathsf{B}^{\mathsf{II}}\,\mathrm{sh}\,\mathsf{K}^* = -(1+\mathsf{R})\left(\mathrm{ch}\,\mathsf{K}^* + e^{\mathsf{i}\mathsf{K}}\right) + 2\mathsf{i}\,\sin\mathsf{K}. \tag{26}$$

   B When $\Omega > 1$, the general solution is given by relation (9). In region II the displacement reads

   $$U^{\mathsf{II}}_j = \mathsf{A}^{\mathsf{II}}\,\mathrm{ch}\,\mathsf{K}^*(j+n+1) + \mathsf{B}^{\mathsf{II}}\,\mathrm{sh}\,\mathsf{K}^*(j+n+1). \tag{27}$$

   Using relation (27) for $j = -n-1$ and $j = -n$ gives $U^{\mathsf{II}}_{-n-1} = \mathsf{A}^{\mathsf{II}}$ and $U^{\mathsf{II}}_{-n} = \mathsf{A}^{\mathsf{II}}\,\mathrm{ch}\,\mathsf{K}^* + \mathsf{B}^{\mathsf{II}}\,\mathrm{sh}\,\mathsf{K}^*$. Comparing with relation (24) one has

   $$\mathsf{A}^{\mathsf{II}} = 1 + \mathsf{R} \qquad \mathsf{B}^{\mathsf{II}}\,\mathrm{sh}\,\mathsf{K}^* = -(1+\mathsf{R})\left(\mathrm{ch}\,\mathsf{K}^* - e^{\mathsf{i}\mathsf{K}}\right) - 2\mathsf{i}\,\sin\mathsf{K}. \tag{28}$$

3. In the region V, assuming that no wave comes from the right, the displacement can be written as

   $$U^{\mathsf{V}}_j = \mathsf{A}^{\mathsf{V}}\; e^{-\mathsf{i}\mathsf{K}(j-n-1)}, \quad j \ge +n \tag{29}$$

   $\mathsf{A}^{\mathsf{V}} = \mathsf{T}$ denoting the amplitude of the transmitted signal. This expression is also valid for $j = +n$, the last point in the region IV of metamaterial. Therefore, one gets

   $$U^{\mathsf{V}}_{+n+1} = \mathsf{T} \qquad U^{\mathsf{V}}_{+n} = \mathsf{T}\, e^{\mathsf{i}\mathsf{K}}. \tag{30}$$

4. In the region IV, as in region II, the general solution of Eq. (6) is given by either relation (9) or (10).

   A When $\Omega < 1$, the general solution is given by relation (10):

   $$U^{\mathsf{IV}}_j = \mathsf{A}^{\mathsf{IV}}\,(-1)^{j-n-1}\mathrm{ch}\,\mathsf{K}^*(j-n-1) + \mathsf{B}^{\mathsf{IV}}\,(-1)^{j-n-1}\mathrm{sh}\,\mathsf{K}^*(j-n-1), \tag{31}$$

   where A^{IV} and B^{IV} have to be determined and $0 \le j \le +n+1$. Using relation (33) for $j = +n+1$ (which corresponds to the first point in the region V) and for $j = +n$, gives $U^{\mathsf{IV}}_{+n+1} = \mathsf{A}^{\mathsf{IV}}$ and $U^{\mathsf{IV}}_{+n} = -\mathsf{A}^{\mathsf{IV}}\,\mathrm{ch}\,\mathsf{K}^* + \mathsf{B}^{\mathsf{IV}}\,\mathrm{sh}\,\mathsf{K}^*$. Comparing with relation (30) one has

   $$\mathsf{A}^{\mathsf{IV}} = \mathsf{T}, \qquad \mathsf{B}^{\mathsf{IV}}\,\mathrm{sh}\,\mathsf{K}^* = \mathsf{T}\left(\mathrm{ch}\,\mathsf{K}^* + e^{\mathsf{i}\mathsf{K}}\right). \tag{32}$$

B When $\Omega > 1$, the general solution is given by relation (9):

$$U_j^{\mathsf{IV}} = \mathsf{A}^{\mathsf{IV}} \operatorname{ch} \mathsf{K}^*(j-n-1) + \mathsf{B}^{\mathsf{IV}} \operatorname{sh} \mathsf{K}^*(j-n-1). \tag{33}$$

Using relation (33) for $j = +n+1$ and for $j = +n$, gives $U_{+n+1}^{\mathsf{IV}} = \mathsf{A}^{\mathsf{IV}}$ and $U_{+n}^{\mathsf{IV}} = \mathsf{A}^{\mathsf{IV}} \operatorname{ch} \mathsf{K}^* - \mathsf{B}^{\mathsf{IV}} \operatorname{sh} \mathsf{K}^*$. Comparing with relation (30) one has

$$\mathsf{A}^{\mathsf{IV}} = \mathsf{T}, \qquad \mathsf{B}^{\mathsf{IV}} \operatorname{sh} \mathsf{K}^* = \mathsf{T}\left(\operatorname{ch} \mathsf{K}^* - e^{\mathsf{i}\mathsf{K}}\right). \tag{34}$$

5. In the region III, the displacement can be written as

$$U_j^{\mathsf{III}} = \mathsf{A}^{\mathsf{III}}\, e^{-\mathsf{i}\mathsf{K}j} + \mathsf{B}^{\mathsf{III}}\, e^{\mathsf{i}\mathsf{K}j}, \quad -1 \le j \le +1 \tag{35}$$

where $\mathsf{A}^{\mathsf{III}}$ and $\mathsf{B}^{\mathsf{III}}$ have to be determined. Applying this expression for $j = -1$ and $j = +1$, one obtains $U_{-1}^{\mathsf{III}} = \mathsf{A}^{\mathsf{III}}\, e^{\mathsf{i}\mathsf{K}} + \mathsf{B}^{\mathsf{III}}\, e^{-\mathsf{i}\mathsf{K}}$ and $U_{+1}^{\mathsf{III}} = \mathsf{A}^{\mathsf{III}}\, e^{-\mathsf{i}\mathsf{K}} + \mathsf{B}^{\mathsf{III}}\, e^{\mathsf{i}\mathsf{K}}$.

We are now able to calculate the displacement of the mass in the defect. In what follows, we only show in detail the calculations for frequencies belonging to band gap A. The same procedure can be also applied for frequencies inside band gap B, with small differences that will result in a slightly changed expression for the displacement of the mass inside the defect (see the final relations (42) and (43)).

Let us impose on the interface between parts II and III and between parts III and IV the conditions corresponding to the the continuity of displacement and stress fields in a continuous medium. One finds:

$$\begin{cases} U_{-1}^{\mathsf{II}} = U_{-1}^{\mathsf{III}} \\ U_0^{\mathsf{II}} = U_0^{\mathsf{III}} \end{cases}, \quad \begin{cases} U_{+1}^{\mathsf{IV}} = U_{+1}^{\mathsf{III}} \\ U_0^{\mathsf{IV}} = U_0^{\mathsf{III}} \end{cases}.$$

From relations (25), (31) and (35), by using relations (26) and (32), these two systems of equations can be rewritten as:

$$\begin{bmatrix} e^{\mathsf{i}\mathsf{K}} & e^{-\mathsf{i}\mathsf{K}} \\ 1 & 1 \end{bmatrix} \begin{bmatrix} \mathsf{A}^{\mathsf{III}} \\ \mathsf{B}^{\mathsf{III}} \end{bmatrix} = \frac{(-1)^n}{\operatorname{sh} \mathsf{K}^*} \begin{bmatrix} -(\mathsf{R}\,\alpha + \overline{\alpha}) \\ \mathsf{R}\,\beta + \overline{\beta} \end{bmatrix} \tag{36}$$

$$\begin{bmatrix} e^{-\mathsf{i}\mathsf{K}} & e^{\mathsf{i}\mathsf{K}} \\ 1 & 1 \end{bmatrix} \begin{bmatrix} \mathsf{A}^{\mathsf{III}} \\ \mathsf{B}^{\mathsf{III}} \end{bmatrix} = \frac{\mathsf{T}\,(-1)^n}{\operatorname{sh} \mathsf{K}^*} \begin{bmatrix} -\alpha \\ \beta \end{bmatrix} \tag{37}$$

with α and β given by:

$$\alpha = \operatorname{sh} \mathsf{K}^*(n-1) + e^{\mathsf{i}\mathsf{K}} \operatorname{sh} \mathsf{K}^* n, \quad \beta = \operatorname{sh} \mathsf{K}^* n + e^{\mathsf{i}\mathsf{K}} \operatorname{sh} \mathsf{K}^*(n+1).$$

From systems (36) and (37) one finds:

$$\begin{cases} \mathsf{A}^{\text{III}} = \dfrac{(-1)^{n+1}}{2\mathrm{i}\,\sin\mathsf{K}\,\mathrm{sh}\,\mathsf{K}^*}\,\{\overline{c} + \mathsf{R}\,d\} \\ \mathsf{B}^{\text{III}} = \dfrac{(-1)^{n}}{2\mathrm{i}\,\sin\mathsf{K}\,\mathrm{sh}\,\mathsf{K}^*}\,\{\overline{d} + \mathsf{R}\,c\} \end{cases} \tag{38}$$

$$\begin{cases} \mathsf{A}^{\text{III}} = \dfrac{\mathsf{T}\,(-1)^{n}}{2\mathrm{i}\,\sin\mathsf{K}\,\mathrm{sh}\,\mathsf{K}^*}\,\{c\} \\ \mathsf{B}^{\text{III}} = \dfrac{\mathsf{T}\,(-1)^{n+1}}{2\mathrm{i}\,\sin\mathsf{K}\,\mathrm{sh}\,\mathsf{K}^*}\,\{d\} \end{cases} \tag{39}$$

with c and d given by:

$$c = \alpha + \beta e^{\mathrm{i}\mathsf{K}}, \quad d = \alpha + \beta e^{-\mathrm{i}\mathsf{K}}.$$

By imposing the equality between the amplitudes A^{III} and B^{III} in (38) and the corresponding ones in (39), R and T can be found from:

$$\begin{bmatrix} d & c \\ c & d \end{bmatrix} \begin{bmatrix} \mathsf{R} \\ \mathsf{T} \end{bmatrix} = - \begin{bmatrix} \overline{c} \\ \overline{d} \end{bmatrix}.$$

The coefficient R of the reflected wave and T of the transmitted wave read

$$\mathsf{R} = \frac{-\overline{c}d + c\overline{d}}{d^2 - c^2}, \qquad \mathsf{T} = \frac{-d\overline{d} + c\overline{c}}{d^2 - c^2}. \tag{40}$$

Finally, the displacement of the point inside the defect takes the form

$$U_0^{\text{III}} = \mathsf{A}^{\text{III}} + \mathsf{B}^{\text{III}}, \tag{41}$$

that, with relations (39) and the second of relations (40), gives

$$U_0^{\text{III}} = \frac{(-1)^n \mathrm{i}\sin\mathsf{K}\,\mathrm{sh}\,\mathsf{K}^*}{\mathrm{sh}\,(n-1)\mathsf{K}^* + (e^{\mathrm{i}\mathsf{K}} + \cos\mathsf{K})\,\mathrm{sh}\,n\mathsf{K}^* + e^{\mathrm{i}\mathsf{K}}\cos\mathsf{K}\,\mathrm{sh}\,(n+1)\mathsf{K}^*}. \tag{42}$$

Relation (42), as stated before, is valid for frequencies belonging to band gap A. When band gap B is considered, U_0^{III} slightly changes and is given by

$$U_0^{\text{III}} = \frac{\mathrm{i}\sin\mathsf{K}\,\mathrm{sh}\,\mathsf{K}^*}{\mathrm{sh}\,(n-1)\mathsf{K}^* - (e^{\mathrm{i}\mathsf{K}} + \cos\mathsf{K})\,\mathrm{sh}\,n\mathsf{K}^* + e^{\mathrm{i}\mathsf{K}}\cos\mathsf{K}\,\mathrm{sh}\,(n+1)\mathsf{K}^*}. \tag{43}$$

4. Energy localization inside the defect

We consider the localization of energy inside the "defect" for the discrete model shown in figure 5. Specifically, our aim is that of comparing the case where attenuation is predominantly due to a Bragg scattering phenomenon, with the case mainly characterized by local resonances.

In the subsequent calculations, we make use of the following relation for the time average of a harmonically varying quantity $u = U\exp\mathrm{i}\omega t$:

$$\langle(\mathcal{R}e(u))^2\rangle = \frac{1}{2}\,U\,\overline{U} = \frac{1}{2}\,|U|^2. \tag{44}$$

4.1. Mechanical energy of the barriers

The mechanical energy density of the barriers e_j^i, with $i = \mathsf{II}, \mathsf{IV}$ and j denoting the $j-th$ mass m_1, is the sum of the potential energy density $\mathcal{W}_j^i$ and the kinetic energy density $\mathcal{K}_j^i$, that are given by:

$$\begin{cases} \mathcal{W}_j^i = \dfrac{1}{2\ell}\left\{\dfrac{k_1}{2}\left[\mathcal{R}e(u_{j+1}^i - u_j^i)\right]^2 + \dfrac{k_1}{2}\left[\mathcal{R}e(u_j^i - u_{j-1}^i)\right]^2 + k_2\left[\mathcal{R}e(v_j^i - u_j^i)\right]^2\right\} \\ \mathcal{K}_j^i = \dfrac{1}{2\ell}\left\{m_1\left[\mathcal{R}e(\dot{u}_j^i)\right]^2 + m_2\left[\mathcal{R}e(\dot{v}_j^i)\right]^2\right\} \end{cases}. \tag{45}$$

Normalizing relations (45) with $k_2\ell$, the dimensionless mechanical energy density $\gamma_j^i = e_j^i/(k_2\ell)$ can be found. Using relation (44) for averaging with respect to time relations (45) and taking into account Eq. (5), the dimensionless averaged mechanical energy density $\langle\gamma_j^i\rangle$ can be written as

$$\langle\gamma_j^i\rangle = \frac{1}{4\ell^2}\left\{\frac{\varepsilon^2}{2}\left[\left|U_{j+1}^i - U_j^i\right|^2 + \left|U_j^i - U_{j-1}^i\right|^2\right] + \left[\mu_\theta + \frac{2\Omega^2}{(1-\Omega)^2}\right]\left|U_j^i\right|^2\right\}, \tag{46}$$

with $i = \mathsf{II}, \mathsf{IV}$ and j denoting the $j-th$ mass m_1.

As shown previously, the motion U_j^i of the j^{th} mass m_1 belonging to the $i-th$ part depends on whether the frequency of the incoming wave belongs to band gap A or B. Therefore, inserting either relations (25) and (31) or (27) and (33) in relation (46), the averaged mechanical energy density in the two cases can be expressed as follows:

- Band gap A.

$$\begin{aligned} \langle\gamma_j^i\rangle = &\frac{1}{4\ell^2}\left\{\left(\mu_\theta + \frac{\Omega^2}{(1-\Omega)^2}\right)\left[\left|\mathsf{A}^i\right|^2 - \left|\mathsf{B}^i\right|^2\right]\right. \\ &+ \left(\frac{1+\operatorname{ch}\mathsf{K}^*}{2} + \frac{\Omega^2}{(1-\Omega)^2}\right)\left[\left(\left|\mathsf{A}^i\right|^2 + \left|\mathsf{B}^i\right|^2\right)\operatorname{ch} 2\mathsf{K}^* s\right. \\ &\left.\left. + 2\left(\mathcal{R}e(\mathsf{A}^i)\mathcal{R}e(\mathsf{B}^i) + \mathcal{I}m(\mathsf{A}^i)\mathcal{I}m(\mathsf{B}^i)\right)\operatorname{sh} 2\mathsf{K}^* s\right]\right\} \end{aligned} \tag{47}$$

- Band gap B.

$$\begin{aligned} \langle\gamma_j^i\rangle = &\frac{1}{4\ell^2}\left\{\left(\mu_\theta + \frac{\Omega^2}{(1-\Omega)^2}\right)\left[\left|\mathsf{A}^i\right|^2 - \left|\mathsf{B}^i\right|^2\right]\right. \\ &+ \left(\frac{1-\operatorname{ch}\mathsf{K}^*}{2} + \frac{\Omega^2}{(1-\Omega)^2}\right)\left[\left(\left|\mathsf{A}^i\right|^2 + \left|\mathsf{B}^i\right|^2\right)\operatorname{ch} 2\mathsf{K}^* s\right. \\ &\left.\left. + 2\left(\mathcal{R}e(\mathsf{A}^i)\mathcal{R}e(\mathsf{B}^i) + \mathcal{I}m(\mathsf{A}^i)\mathcal{I}m(\mathsf{B}^i)\right)\operatorname{sh} 2\mathsf{K}^* s\right]\right\} \end{aligned} \tag{48}$$

with

$$\begin{cases} i = \mathsf{II} \text{ and } s = j + n + 1 \\ i = \mathsf{IV} \text{ and } s = j - n - 1 \end{cases}.$$

4.2. Mechanical energy of the mass-spring chain

The dimensionless averaged mechanical energy density $\langle \gamma_j \rangle$ of the j^{th} unit cell for a mass-spring chain (regions I, III and IV of the system) is given by:

$$\langle \gamma_j^i \rangle = \frac{1}{4\ell^2} \left\{ \frac{\varepsilon^2}{2} \left| U_{j+1}^i - U_j^i \right|^2 + \frac{\varepsilon^2}{2} \left| U_j^i - U_{j-1}^i \right|^2 + \Omega\theta \left| U_j^i \right|^2 \right\}, \tag{49}$$

with $i = \mathsf{I}, \mathsf{III}, \mathsf{V}$. The motion U_j^i of the j-th mass m_1 is obtained either from relation (23), (29) or (35). Inserting these latter relations into (49), one obtains:

$$\begin{aligned} \langle \gamma_j^i \rangle = & \frac{2\varepsilon^2}{\ell^2} \sin^2 \frac{\mathsf{K}}{2} \Big\{ \Big[\left| \mathsf{A}^i \right|^2 + \left| \mathsf{B}^i \right|^2 \Big] \\ & + (1 - \cos \mathsf{K}) \Big[\big(\mathcal{R}e(\mathsf{A}^i)\mathcal{R}e(\mathsf{B}^i) + \mathcal{I}m(\mathsf{A}^i)\mathcal{I}m(\mathsf{B}^i) \big) \cos 2\mathsf{K}j \\ & + \big(\mathcal{I}m(\mathsf{A}^i)\mathcal{R}e(\mathsf{B}^i) - \mathcal{R}e(\mathsf{A}^i)\mathcal{I}m(\mathsf{B}^i) \big) \sin 2\mathsf{K}j \Big] \Big\}, \end{aligned} \tag{50}$$

with A^i and B^i denoting the wave amplitudes for the $i-th$ part, with $i = \mathsf{I}, \mathsf{III}, \mathsf{V}$, and where we have used relation (18). Note that the defect (region III) is composed by a single cell, therefore only $j = 0$ is considered.

4.3. The localization phenomenon

Let us now consider the localization phenomenon. By tuning the parameters governing the problem, it is possible to exploit either a Bragg or a locally resonant behaviour for focusing inside the defect the energy carried by an incoming wave. Specifically, as shown in figures 3 and 4, the two attenuating mechanisms can be activated depending on the values chosen for θ and ε. The number n of unit cells composing each barrier only modifies the efficacy of the attenuation generated by the barriers and, hence, it can be fixed without varying the width of band gaps A and B.

In what follows, we fix $n = 2$ and discuss several systems characterized by different θ and ϵ. Selecting *e.g.* $\theta = 1$ and looking at figure 6a, depending on ε the system can work either with Ω belonging only to band gap A, to band gap A and B, or only to band gap B. Specifically, one has:

$$\begin{cases} \varepsilon^2 \leq \theta/4 & \text{only band gap A} \\ \theta/4 < \varepsilon^2 < \mathcal{O}(1) & \text{band gaps A and B} \\ \varepsilon^2 >> 1 & \text{only band gap B} \end{cases}$$

Therefore, the following three cases are analysed: $\varepsilon = 0.4$, $\varepsilon = 1$ and $\varepsilon = 3$ (this latter value is high enough to consider the problem governed only by band gap B).

By employing relations (50) and (18), the averaged mechanical energy density of the unit cell composing the defect $\langle \gamma_0^{\mathsf{III}} \rangle$, normalized with respect to the incoming energy $\langle \gamma_{in} \rangle$, can be plotted as a function of the frequency Ω, as shown in figure 7, where a logarithmic scale is used for the vertical axis. More specifically, the energy has been computed only for those frequencies respecting condition (22), which itself depends on ε; for this reason, the

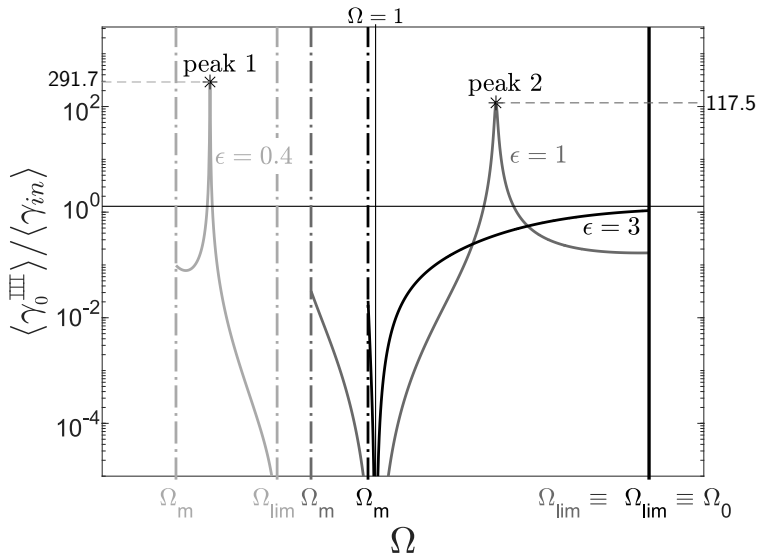

Figure 7: averaged mechanical energy density of the defect $\langle \gamma_0^{III} \rangle$, normalized with respect to $\langle \gamma_{in} \rangle$ (*i.e.* the energy carried by the incoming wave) versus frequency Ω for: $\varepsilon = 0.4$ (light gray), $\varepsilon = 1$ (gray) and $\varepsilon = 3$ (black). A logarithmic scale is used for the vertical axis. The vertical dashed-dotted lines delimit the intervals of frequencies Ω respecting condition (22) for each of the three considered ε. The vertical line at $\Omega = 1$ separates band gap A from band gap B. When $\varepsilon = 3$, the normalized energy density is not experiencing any peak and is smaller than 1 $\forall\Omega$ respecting condition (22).

intervals of frequencies between Ω_m and Ω_{lim} vary for the three cases. From figure 7, for $\varepsilon = 0.4$ and $\varepsilon = 1$ a peak appears ("peak 1" and "peak 2" respectively) that corresponds to a maximum localization of the incoming energy. In general, for Ω belonging to a band gap, the presence of the first barrier generates a reflected wave and, as a consequence, the energy transmitted to the defect should be less than the incoming one ($\langle \gamma_0^{III} \rangle / \langle \gamma_{in} \rangle \leq 1$). The presence of a peak greater than 1 confirms that the introduction of a defect gives rise to a peculiar behaviour, causing an accumulation of the energy traveling along the system. Nevertheless, the localization doesn't always take place, as one can verify by looking at the behaviour of $\langle \gamma_0^{III} \rangle / \langle \gamma_{in} \rangle$ for $\varepsilon = 3$ (see figure 7): for this particular value, no peaks are present.

"Peak 1" and "peak 2" appear respectively at $\Omega = 0.394$ and $\Omega = 1.440$. Considering these two frequencies, the normalized energy $\langle \gamma_j \rangle / \langle \gamma_{in} \rangle$ along the entire system is shown in figure 8 ($j \in \mathbb{Z}$ indicates the j^{th} unit cell).

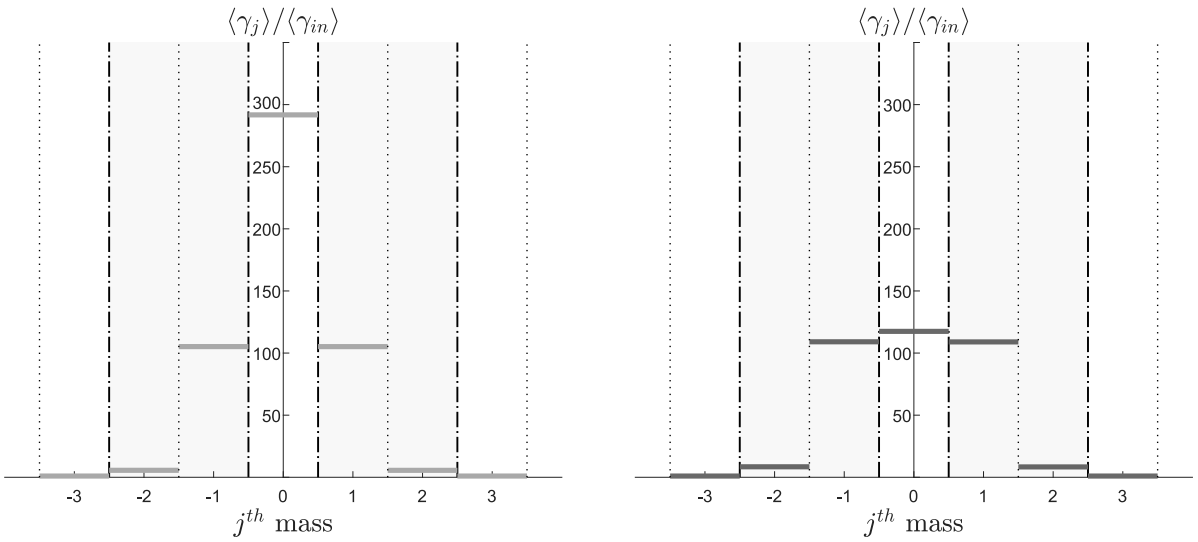

(a) (b)

Figure 8: mechanical energy density γ^j of each unit cell j composing the system, averaged over a time period and normalized with respect to the incoming one, for Ω corresponding to "peak 1" (figure 8a) and "peak 2" (figure 8b). The vertical dotted lines are used to separate the different unit cells; moreover, the dashed-dotted vertical lines delimit the two barriers in both figures.

The behaviour of the system is very similar for the two cases, although the level of concentration for $\varepsilon = 0.4$ (figure 8a) is higher than that of $\varepsilon = 1$ (figure 8b). This aspect can also be quantified by introducing an index of concentration (IC), defined as follows:

$$IC = \frac{\langle E^{\text{III}} \rangle}{\langle E^{\text{II}} \rangle + \langle E^{\text{III}} \rangle + \langle E^{\text{IV}} \rangle}, \tag{51}$$

with E^i denoting the total mechanical energy of the i^{th} part, simply given by $E^i = \ell \sum_j \gamma_j \, k_2 \ell$, for $j \in$ part i^{th} (this means that the sum considers all the unit cells j composing the i^{th} part). Using this index for peaks 1 and 2, one obtains respectively $IC_1 = 0.57$ and $IC_2 = 0.33$, thus confirming a larger localization for $\varepsilon = 0.4$.

Since "peak 1" belongs to band gap A and "peak 2" to band gap B, the above analysis shows that both Bragg scattering and local resonance can generate a localization phenomenon.

4.4. Motion of the mass in the defect

Let us now study the motion U_0^{III} of the mass inside the defect and how its presence affects the transmission coefficient T. In particular, by using the second of relations (40) and (41), both quantities can be expressed for varying frequencies. This is shown in figures 9a and 9b, where we plot respectively $\left|U_0^{\text{III}}(\Omega)\right| / |U_{in}|$ (U_{in} is the motion imposed in part I by the incoming wave) and $|\mathsf{T}(\Omega)|$, again only for those frequencies verifying condition (22), for each ε. In figure 9a, a logarithmic scale is used for the vertical axis.

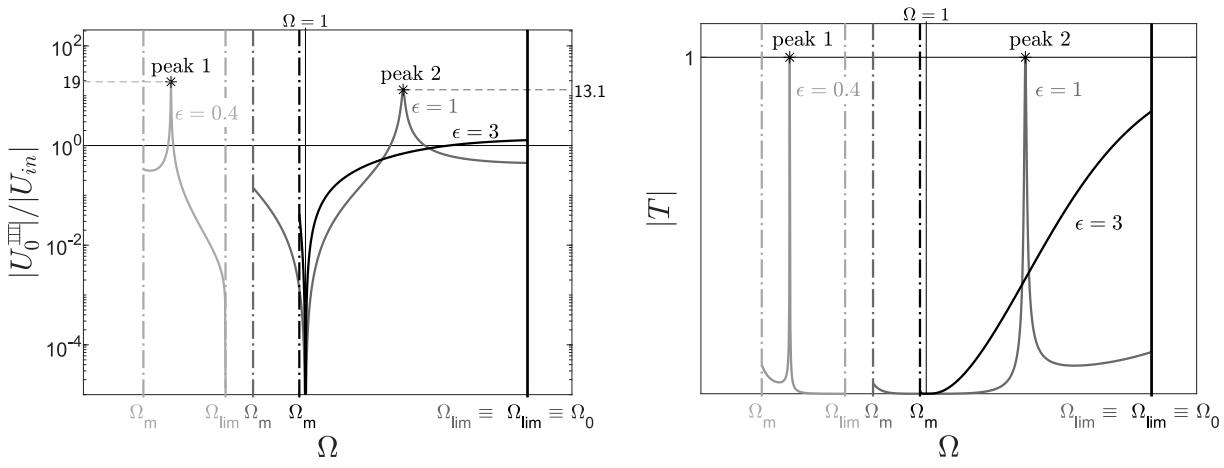

Figure 9: (a) Displacement magnitude $\left|U_0^{\text{III}}\right|$ of the mass inside the defect normalized with the amplitude $|U_{in}|$ of the incoming wave, as a function of Ω. A logarithmic scale is used for the vertical axis. (b) Modulus $|\mathsf{T}|$ of the transmission coefficient versus Ω. The different colors refer to the three different ε (light gray: $\varepsilon = 0.4$, gray: $\varepsilon = 1$, black: $\varepsilon = 3$).

When $\varepsilon = 0.4$ and $\varepsilon = 1$, both plots in figure 9 present one peak, exactly at the same frequency where $\langle\gamma_0^{\text{III}}(\Omega)\rangle/\langle\gamma_{in}\rangle$ is maximum. These frequencies also correspond to perfect transmission (*i.e.* $|\mathsf{T}| = 1$): this is another peculiarity introduced by the presence of a defect. A similar result was found by the authors for a continuum case (see [47, 48]).

4.5. Localization in the time domain

Up to now, we have only considered the behaviour of the system at its steady state for a given frequency. Here we also analyse the problem in the time domain, by means of a centered finite difference scheme and we check that, for $\varepsilon = 0.4$ and $\varepsilon = 1$ and for a time t large enough, $\left|U_0^{\text{III}}(t)\right| / |U_{in}|$ tends to the peak values shown in figure 9a and $|\mathsf{T}(t)| \approx 1$ ($|U_{in}|$ is not a function of t because it is imposed to be constant).

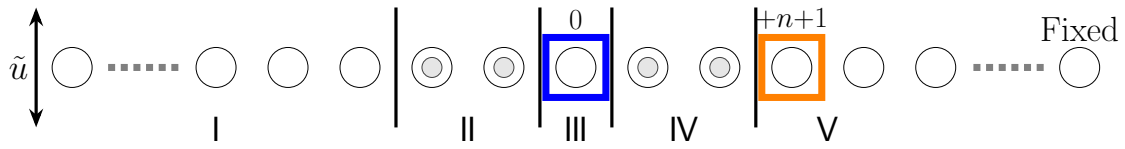

Figure 10: sketch of the system used for the time domain analysis. Parts I and V are now of finite thickness. The first mass on the left is subjected to an imposed displacement $\tilde{u} = \sin\omega t$, with $\omega = \sqrt{\overline{\Omega}}\,\omega_2$ and $\overline{\Omega}$ denoting the peak frequency under consideration. The last mass on the right is fixed. Masses $j = 0$ (blue) and $j = +n+1$ (orange) are evidenced for later use.

Figure 10 schematically represents the system used for the time domain analysis. In order to carry out a numerical solution of the problem, we considered finite dimensions for parts I and V and we imposed boundary conditions on the first and final mass respectively of parts I and V. In particular, the motion of the first mass on the left is constraint to be

$\tilde{u} = \sin \omega t$ (the amplitude of the generated incoming wave is hence equal to 1, $|U_{in}| = 1$), with $\omega = \sqrt{\overline{\Omega}}\omega_2$, where $\overline{\Omega}$ is the frequency of the peaks computed in the previous section; the last mass on the right instead is fixed. By choosing the properties of the resonator (mass m_2 and spring k_2), ω_2 is defined and thus also ω. The two quantities of interest, namely $\left|U_0^{\text{III}}(t)\right|$ and $|\mathsf{T}(t)|$, are the amplitudes, for large t, of displacements $|u_0(t)|$ and $|u_{+n+1}(t)|$ of the masses highlighted respectively in orange and blue in figure 10. They can be derived by analysing the motion of the two masses with respect to time, as shown in figures 11a ($\varepsilon = 0.4$) and 12a ($\varepsilon = 1$). The amplitude $|u_0(t)|$ at large t almost coincides with the corresponding value $\left|U_0^{\text{III}}(\Omega)\right|$ shown in figure 9a, for both peaks; moreover, again for large t, the amplitude $|u_{+n+1}(t)|$ of the transmitted wave tends to 1. This verifies the localization phenomenon and quantifies the time frame Δt, which is necessary for the system to reach the maximum level of concentration. More in details, the transitory time Δt depends on the final level of energy concentration inside the cavity, when a stationary condition is reached. The higher is the energy peak in figure 7, the larger will be the time needed for reaching the final regime. This is shown in figures 11a and 12a: the transitory time for "peak 1" is larger with respect to that related to "peak 2". As the level of concentration depends on the level of attenuation provided by the barriers at the frequency corresponding to a peak of energy, the transitory time is indirectly influenced by both the stiffness and mass ratios.

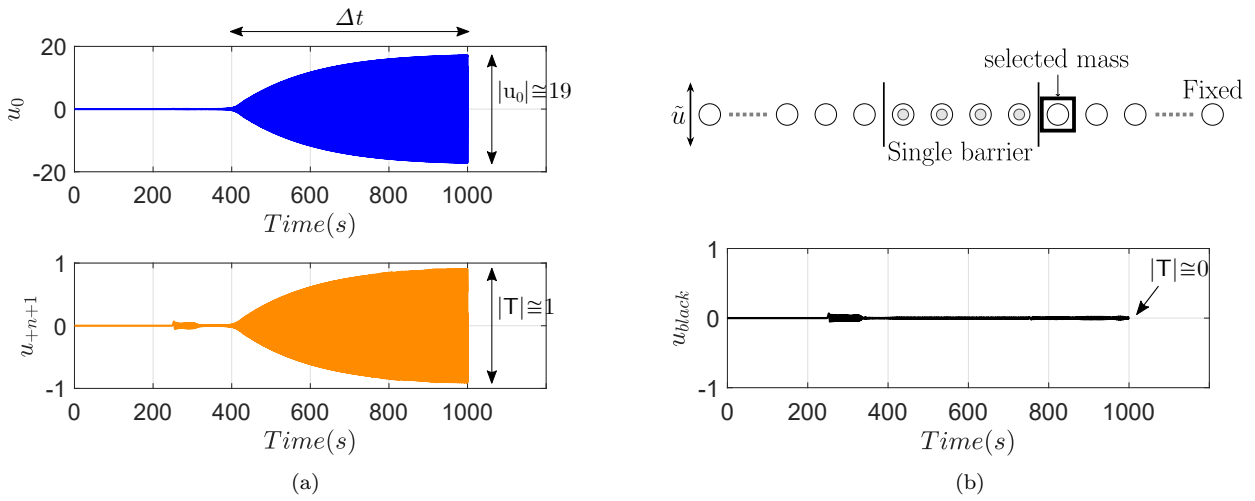

Figure 11: (a) Oscillations in time of displacements u_0 and u_{+n+1} of the masses evidenced respectively in blue and orange in figure 10. (b) Oscillation in time of the displacement of the first cell after a barrier without defect (sketch above). Material parameters: $\theta = 1$, $\varepsilon = 0.4$, $m_2 = 0.01$ Kg, $k_2 = 1$ N m^{-1}.

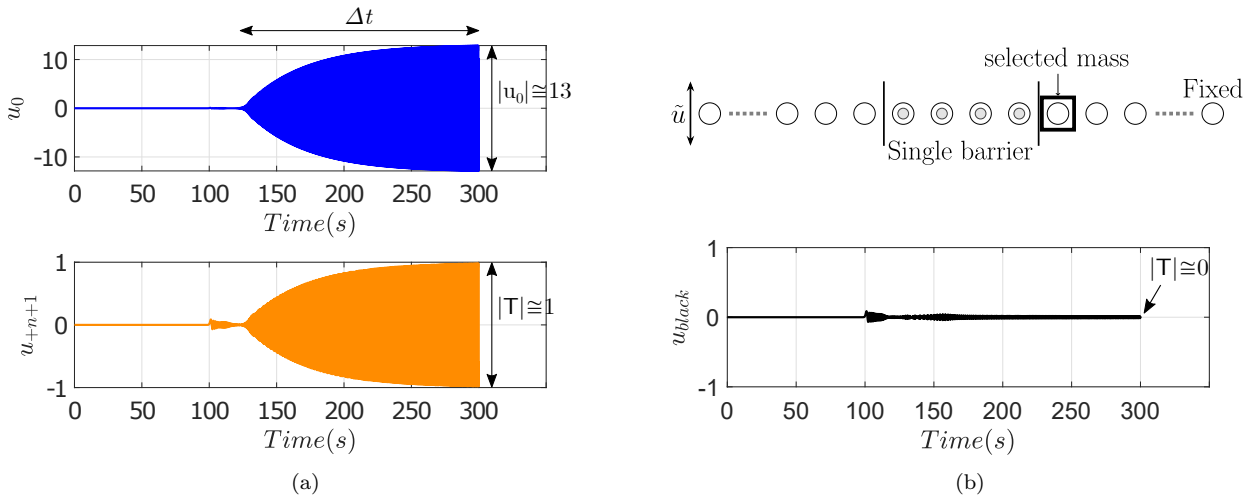

Figure 12: (a) Oscillations in time of displacements u_0 and u_{+n+1} of the masses evidenced respectively in blue and orange in figure 10. (b) Oscillation in time of the displacement of the first cell after a barrier without defect (sketch above). Material parameters: $\theta = 1$, $\varepsilon = 1$, $m_2 = 0.01$ Kg, $k_2 = 1$ N m^{-1}.

An important remark is here necessary: the presence of boundaries could affect the result by generating reflected waves that, nevertheless, need some time to reach the two masses of interest. Therefore, by tuning the total time of the analysis in relation to the speed of the traveling waves and the number of unit cells used in parts I and V, it is possible to neglect the presence of these reflected waves.

The influence of the defect can be finally evidenced by considering the system schematically depicted in figures 11b, 12b (above) and analysing the amplitude $|u_{black}(t)|$ of the transmitted wave, *i.e.* the amplitude of the motion of the mass evidenced in black in the figures. The system is composed by a mass-spring chain with a single barrier of 4 cells without defect. For this system the transmitted wave amplitude is almost zero for both ε, as shown in figures 11b and 12b (below). This final result confirms the substantial change of behaviour with respect to the case with the defect.

5. Concluding remarks

Mass-in-mass discrete systems have been widely studied and employed to represent the behaviour of LRMs. This work has highlighted that this lattice actually represents a *hybrid metamaterial* that can be tuned to behave either as a PC or as a LRMs. The two parameters of the problem, namely the ratio between the stiffnesses and that between the masses, influence the wave cancelling capacity of the mass-in-mass chain. The variation of the band gaps position and width is due to the activation of the mechanisms of Bragg scattering or local resonance.

The present study of the effective model built from the discrete HM has set the limit of validity of the method based on the negative effective mass, method which is generally used in literature to determine band gaps in discrete systems. The limit is related to the ratio between the stiffness of the chain and that of the resonators.

The attenuating capabilities have been exploited to study a discrete system for the harvesting of energy carried by a propagating wave. Introducing a defect in the mass-in-mass chain, waves can be localized and the energy that they transport can be focused. The analytical treatment allowed to derive the optimal conditions for energy localization. A worth noting result is that the Bragg scattering offers a better response in terms of energy concentration.

All the analytical results have been verified through computations in the time domain.

We remark that, having considered a one-dimensional problem, the context has been that of scalar waves, but exactly the same considerations would apply in more dimensions. Furthermore, the results obtained can be employed for other problems that can be brought back to the solution of discrete differential equations of the type studied here. A work in this direction is currently in progress.

Acknowledgements

The second Author wishes to thank the Colleagues of École polytechnique for kind hospitality and the Laboratoire de Mécanique des Solides, for financial support.

References

[1] J. D. Joannopoulos, S. G. Johnson, J. N. Winn, R. D. Meade, Photonic Crystals: Molding the Flow of Light (Second Edition), Princeton University Press, 2008.

[2] P. A. Deymier (Ed.), Acoustic Metamaterials and Phononic Crystals, volume 173 of *Springer Series in Solid-State Sciences*, Springer Berlin Heidelberg, Berlin, Heidelberg, 2013.

[3] V. Laude, Phononic Crystals, DE GRUYTER, Berlin, München, Boston, 2015.

[4] M.-H. Lu, L. Feng, Y.-F. Chen, Phononic crystals and acoustic metamaterials, Mater. Today 12 (2009) 34–42.

[5] R. De, L. K. Bo, Quantum mechanics of electrons in crystal lattices, Proc. R. Soc. London. Ser. A, Contain. Pap. a Math. Phys. Character 130 (1931) 499–513.

[6] C. Goffaux, J. Sánchez-Dehesa, A. L. Yeyati, P. Lambin, A. Khelif, J. O. Vasseur, B. Djafari-Rouhani, Evidence of Fano-like interference phenomena in locally resonant materials, Phys. Rev. Lett. 88 (2002) 225502/1–225502/4.

[7] M. F. Limonov, M. V. Rybin, A. N. Poddubny, Y. S. Kivshar, Fano resonances in photonics, Nat. PHOTONICS — 11 (2017).

[8] G. W. Milton, J. R. Willis, On modifications of Newton's second law and linear continuum elastodynamics, Proc. R. Soc. A Math. Phys. Eng. Sci. 463 (2007) 855–880.

[9] K. Pham, A. Maurel, J. J. Marigo, Two scale homogenization of a row of locally resonant inclusions - the case of anti-plane shear waves, J. Mech. Phys. Solids 106 (2017) 80–94.

[10] X. Hu, C. T. Chan, J. Zi, Two-dimensional sonic crystals with Helmholtz resonators, Phys. Rev. E - Stat. Nonlinear, Soft Matter Phys. 71 (2005) 1–4.

[11] C. Boutin, F. X. Becot, Theory and experiments on poro-acoustics with inner resonators, Wave Motion 54 (2015) 76–99.

[12] K. Pham, J. F. Mercier, D. Fuster, J. J. Marigo, A. Maurel, Scattering of acoustic waves by a nonlinear resonant bubbly screen, J. Fluid Mech. (2020).

[13] N. Kaina, M. Fink, G. Lerosey, Composite media mixing Bragg and local resonances for highly attenuating and broad bandgaps, Sci. Rep. 3 (2013) 3240.

[14] B. Yuan, V. F. Humphrey, J. Wen, X. Wen, On the coupling of resonance and Bragg scattering effects in three-dimensional locally resonant sonic materials, Ultrasonics 53 (2013) 1332–1343.

[15] A. O. Krushynska, M. Miniaci, F. Bosia, N. M. Pugno, Coupling local resonance with Bragg band gaps in single-phase mechanical metamaterials, Extrem. Mech. Lett. 12 (2017) 30–36.
[16] J. S. Jensen, Phononic band gaps and vibrations in one- and two-dimensional mass-spring structures, J. Sound Vib. 266 (2003) 1053–1078.
[17] L. Brillouin, Wave Propagation in Periodic Structures - Electric Filters and Crystal Lattices, 1 ed., McGraw - Hill Book Company, Inc., 1946.
[18] A. S. Fallah, Y. Yang, R. Ward, M. Tootkaboni, R. Brambleby, A. Louhghalam, L. A. Louca, Wave propagation in two-dimensional anisotropic acoustic metamaterials of K4 topology, Wave Motion 58 (2015) 101–116.
[19] X. An, H. Fan, C. Zhang, Elastic wave and vibration bandgaps in two-dimensional acoustic metamaterials with resonators and disorders, Wave Motion 80 (2018) 69–81.
[20] C. Comi, L. Driemeier, Wave propagation in cellular locally resonant metamaterials, Lat. Am. J. Solids Struct. 15 (2018).
[21] M. Jaberzadeh, B. Li, K. T. Tan, Wave propagation in an elastic metamaterial with anisotropic effective mass density, Wave Motion 89 (2019) 131–141.
[22] Y. Y. Chen, M. V. Barnhart, J. K. Chen, G. K. Hu, C. T. Sun, G. L. Huang, Dissipative elastic metamaterials for broadband wave mitigation at subwavelength scale, Compos. Struct. 136 (2016) 358–371.
[23] P. P. Kulkarni, J. M. Manimala, Longitudinal elastic wave propagation characteristics of inertant acoustic metamaterials, J. Appl. Phys. 119 (2016).
[24] N. M. Frandsen, J. S. Jensen, Modal interaction and higher harmonic generation in a weakly nonlinear, periodic mass–spring chain, Wave Motion 68 (2017) 149–161.
[25] T. U. R. Abbasi, H. Zheng, Wave dispersion and dissipation performance of locally resonant acoustic metamaterials using an internal variable model, Wave Motion 93 (2020) 102483.
[26] S. Yao, X. Zhou, G. Hu, Experimental study on negative effective mass in a 1D mass–spring system, New J. Phys. 10 (2008) 043020.
[27] H. H. Huang, C. T. Sun, G. L. Huang, On the negative effective mass density in acoustic metamaterials, Int. J. Eng. Sci. 47 (2009) 610–617.
[28] H. H. Huang, C. T. Sun, Wave attenuation mechanism in an acoustic metamaterial with negative effective mass density, New J. Phys. 11 (2009).
[29] J.-L. Auriault, C. Boutin, Long wavelength inner-resonance cut-off frequencies in elastic composite materials, Int. J. Solids Struct. 49 (2012) 3269–3281.
[30] C. Comi, J.-J. Marigo, Homogenization Approach and Bloch-Floquet Theory for Band-Gap Prediction in 2D Locally Resonant Metamaterials, J. Elast. 139 (2020) 61–90.
[31] C. Comi, M. Moscatelli, J.-J. Marigo, Two scale homogenization in ternary locally resonant metamaterials, Mater. Phys. Mech. 44 (2019) 8–18.
[32] W. J. Parnell, T. Shearer, Antiplane elastic wave cloaking using metamaterials, homogenization and hyperelasticity, Wave Motion 50 (2013) 1140–1152.
[33] S. J. Mitchell, A. Pandolfi, M. Ortiz, Metaconcrete: Designed aggregates to enhance dynamic performance, J. Mech. Phys. Solids 65 (2014) 69–81.
[34] R. Schittny, M. Kadic, S. Guenneau, M. Wegener, Experiments on transformation thermodynamics: Molding the flow of heat, Phys. Rev. Lett. 110 (2013).
[35] J. Jung, H.-G. Kim, S. Goo, K.-J. Chang, S. Wang, Realisation of a locally resonant metamaterial on the automobile panel structure to reduce noise radiation, Mech. Syst. Signal Process. 122 (2019) 206–231.
[36] E. W. Montroll, R. B. Potts, Effect of defects on lattice vibrations, Phys. Rev. 100 (1955) 525–543.
[37] A. A. Maradudin, Some effects of point defects on the vibrations of crystal lattices, Reports Prog. Phys. 28 (1965) 331–380.
[38] M. M. Sigalas, Elastic wave band gaps and defect states in two-dimensional composites, J. Acoust. Soc. Am. 101 (1997) 1256–1261.
[39] M. M. Sigalas, Defect states of acoustic waves in a two-dimensional lattice of solid cylinders, J. Appl.

Phys. 84 (1998) 3026–3030.
[40] F. Wu, Z. Hou, Z. Liu, Y. Liu, Point defect states in two-dimensional phononic crystals, Phys. Lett. Sect. A Gen. At. Solid State Phys. 292 (2001) 198–202.
[41] L. Y. Wu, L. W. Chen, Wave propagation in a 2D sonic crystal with a Helmholtz resonant defect, J. Phys. D. Appl. Phys. 43 (2010).
[42] L. Y. Wu, L. W. Chen, C. M. Liu, Acoustic energy harvesting using resonant cavity of a sonic crystal, Appl. Phys. Lett. 95 (2009).
[43] H. Lv, X. Tian, M. Y. Wang, D. Li, Vibration energy harvesting using a phononic crystal with point defect states, Appl. Phys. Lett. 102 (2013) 2013–2016.
[44] X. F. Lv, X. Fang, Z. Q. Zhang, Z. L. Huang, K. C. Chuang, Highly localized and efficient energy harvesting in a phononic crystal beam: Defect placement and experimental validation, Crystals 9 (2019).
[45] S.-H. Jo, H. Yoon, Y. C. Shin, M. Kim, B. D. Youn, Elastic wave localization and harvesting using double defect modes of a phononic crystal, J. Appl. Phys. 127 (2020) 164901.
[46] S. H. Jo, H. Yoon, Y. C. Shin, W. Choi, C. S. Park, M. Kim, B. D. Youn, Designing a phononic crystal with a defect for energy localization and harvesting: Supercell size and defect location, Int. J. Mech. Sci. 179 (2020).
[47] M. Moscatelli, C. Comi, J.-J. Marigo, Locally Resonant Materials for Energy Harvesting at Small Scale, in: Proc. XXIV AIMETA Conf. 2019, September, Rome, 2020, pp. 606–626.
[48] M. Moscatelli, C. Comi, J.-J. Marigo, Energy Localization through Locally Resonant Materials, Materials (Basel). 13 (2020) 3016.
[49] S. H. Jo, H. Yoon, Y. C. Shin, B. D. Youn, An analytical model of a phononic crystal with a piezoelectric defect for energy harvesting using an electroelastically coupled transfer matrix, Int. J. Mech. Sci. 193 (2021) 106160.
[50] T. Terao, Wave propagation in acoustic metamaterial double-barrier structures, Phys. Status Solidi Appl. Mater. Sci. 213 (2016) 2773–2779.